

*Chapter 6***ROTATION CURVES IN BOSE-EINSTEIN
CONDENSATE DARK MATTER HALOS***M. Dwornik, Z. Keresztes, L. Á. Gergely**Department of Theoretical Physics, University of Szeged,
Tisza Lajos krt 84-86, Szeged 6720, HungaryDepartment of Experimental Physics, University of Szeged,
Dóm Tér 9, Szeged 6720, Hungary**1. ABSTRACT**

The study of the rotation curves of spiral galaxies reveals a nearly constant cored density distribution of Cold Dark Matter. N-body simulations however lead to a cuspy distribution on the galactic scale, with a central peak. A Bose-Einstein condensate (BEC) of light particles naturally solves this problem by predicting a repulsive force, obstructing the formation of the peak. After succinctly presenting the BEC model, we test it against rotation curve data for a set of 3 High Surface Brightness (HSB), 3 Low Surface Brightness (LSB) and 3 dwarf galaxies. The BEC model gives a similar fit to the Navarro-Frenk-White (NFW) dark matter model for all HSB and LSB galaxies in the sample. For dark matter dominated dwarf galaxies the addition of the BEC component improved more upon the purely baryonic fit than the NFW component. Thus despite the sharp cut-off of the halo density, the BEC dark matter candidate is consistent with the rotation curve data of all types of galaxies.

2. INTRODUCTION

Cosmological observations provide compelling evidence that about 95% of the content of the Universe resides in the unknown dark matter and dark energy components [60]. The former resides in bound systems as non-luminous matter [57,68], the latter in the form of a zero-point energy pervading the whole Universe. Dark matter is thought to be composed of pressureless, cold, neutral, weakly interacting massive particles, beyond those existing in

*E-mail address: gergely@physx.u-szeged.hu

the Standard Model of Particle Physics, and not yet detected in accelerators or in dedicated direct and indirect searches, excepting gravitational has been found. Therefore the possibility that the Einstein (and Newtonian) theory of gravity breaks down at the scale of galaxies cannot be excluded a priori. While some studies show that the luminous matter alone can explain the rotation in the innermost galactic regions [20,54,70], dark matter is still required on the larger scale. Several theoretical models, based on a modification of Newton's law or of general relativity, have been proposed to explain the behavior of the galactic rotation curves [5–8, 46, 50, 51, 64, 67]. In brane world models, the galactic rotation curves can be naturally explained without introducing dark matter [24, 45, 62]. There is also a possibility that the rotation of galaxies in the outermost regions could be driven by magnetic fields, rather than dark matter [3].

In recent cosmological models the primordial density fluctuations are generated during an inflationary period and they are the seeds of the bottom-up structure formation model. The post-inflation regime is usually described by the Λ CDM (cosmological constant + Cold Dark Matter) model which is consistent with the vast majority of the available observations, including the large scale matter distribution, the Ia type supernovae observations and the temperature fluctuations in the cosmic microwave background radiation [55, 56, 61].

However, the investigation of spiral galaxies clearly shows that the mass distribution of galactic-scale objects can not be explain satisfactory within the framework of the Λ CDM cosmological model. The predicted halo density profile is approximately isothermal over a large range in radii, and it shows a well pronounced central cusp [52]. The Navarro-Frenk-White (NFW) density profile is proportional to $1/r$ close to the centre. On the observational side however, high-resolution rotation curves show instead that the actual distribution of dark matter is much shallower [11], presenting a constant density core. The Burkert density profile shows a correlation between the enclosed surface densities of luminous and dark matter in galaxies [23]. However the astrophysical origin of this empirical density distribution remains unaddressed.

The knowledge of the mass distribution of spiral galaxies is a crucial step in the search for non-baryonic dark matter. Most of the present models assume that, beside the stellar disk and bulge, there is a spherically symmetric, massive dark matter halo, which dominates the total galaxy mass and also determines the dynamics of the stellar disk at the outer regions. Nevertheless Ref. [37] found that the mass distribution for some galaxies cannot be spherical at larger radii and instead a flattened mass distribution (global disk model) better approximates the gravitational potential.

In this chapter we consider scalar field dark matter halos which have undergone a Bose-Einstein condensation (BEC) [6, 13, 14, 21, 33, 34, 63, 72]. Below a critical temperature, bosons favor joining highly populated low-energy states. At the end of this process, bosons will occupy the same quantum ground state and form a coherent matter wave, the Bose-Einstein condensate. In this state, the bosons exhibit a repulsive interaction which prevents the formation of central density cusps by gravitational attraction.

This chapter is organized as follows. The basic properties of the Bose-Einstein condensed dark matter are reviewed in Section 2. Then the theoretical predictions of the model are compared with the observed rotation curve data of several types of galaxies (High Surface Brightness, Low Surface Brightness and Dwarf Galaxies, respectively), in Section 3. We discuss the results in Section 4.

3. THE BOSE-EINSTEIN CONDENSATE

An ideal Bose gas (a cloud of non-interacting bosons) confined in a box of volume $V = L^3$ obeys the Bose-Einstein thermal distribution $f = \{\exp[(\epsilon - \mu)/k_B T] - 1\}^{-1}$, where $\epsilon = p^2/2m$ stands for the energy of the bosons, determined by their mass m and magnitude p of their 3-momentum vector, μ is the chemical potential, T the temperature and k_B the Boltzmann constant. The 3-momentum $\mathbf{p} = 2\pi\hbar\mathbf{q}/L$ is discretized through the dimensionless vector \mathbf{q} , with integer components. The lowest energy state has $p = 0$. The number of uncondensated bosons at temperature T is

$$N_T = \sum_{p \neq 0} \frac{1}{\exp[(p^2/2m - \mu)/k_B T] - 1} . \quad (1)$$

If the energy levels follow each other densely, i.e. the thermal energy is much larger than the smallest energy spacing between the single-particle levels:

$$k_B T \gg \frac{2\pi^2 \hbar^2}{mV^{2/3}} , \quad (2)$$

the summation in Eq. (1) can be replaced by an integral over the momentum ($\sum_{\mathbf{p}} \rightarrow V \int d\mathbf{p}/(2\pi\hbar)^3$) cf. Ref. [59], thus:

$$N_T = \frac{V}{\lambda_T^3} g_{3/2}[\exp(\mu/k_B T)] . \quad (3)$$

Here

$$\lambda_T = \hbar \sqrt{\frac{2\pi}{mk_B T}} \quad (4)$$

is the thermal de Broglie wavelength and

$$g_{3/2}(z) = \frac{2}{\sqrt{\pi}} \int_0^\infty dx \frac{\sqrt{x}}{e^{x/z} - 1} \quad (5)$$

is a special Bose function, with $z = \exp(\mu/k_B T)$ and the integral variable $x = p^2/2mk_B T$. At such temperatures when the ground state is vacant, the value of the chemical potential can be expressed from the relation $N_T = N$, with N the total number of bosons. If the lowest energy state $\epsilon_0 = 0$ is occupied, the chemical potential is given by

$$\mu = -k_B T \ln \left(1 + \frac{1}{n_0} \right) \approx -\frac{k_B T}{n_0} , \quad (6)$$

with the ground state particle number n_0 . In the thermodynamic limit $n_0, N, V \rightarrow \infty$, $n = N/V, n_0/V \rightarrow \text{const}$, such that n_0/N can be expressed as

$$\frac{n_0}{N} = 1 - \left(\frac{T}{T_c} \right)^{3/2} \quad (T \leq T_c) . \quad (7)$$

The critical temperature

$$T_c = \frac{2\pi\hbar^2}{mk_B} \left(\frac{n}{g_{3/2}(0)} \right)^{2/3} , \quad (8)$$

with $g_{3/2}(0) = 2.612$, is typically low ($T_c = 3.13$ K for ^4He liquid at saturated vapour pressure), and represents the temperature below which the bosons start to condensate into the lowest energy state. By further decreasing the temperature, the relative number of particles in the ground state increases. For $T > T_c$ the ground state is vacant.

The condition for the condensation $T < T_c$ can be rewritten as a relation between the average distance of the bosons $l = \sqrt[3]{V/N} = n^{-1/3}$ and their thermal de Broglie wavelength as

$$l < \frac{\lambda_T}{\zeta^{1/3}} \approx 0.73\lambda_T. \quad (9)$$

With the bosons considered a quantum-mechanical wave packet of the order of its de Broglie wavelength, the condensation occurs at the low temperatures where their wavelengths overlap.

As the thermodynamic limit is never realized exactly, corrections arising from the finite size slightly alter the value of the critical temperature, for details see [29], [39], [40], [32].

In a dense, non-ideal (self-interacting) Bose gas the particles can form molecules, and they can reach a more stable state than a BEC. Two atoms can form a molecule if a third particle takes momentum away. In a dilute gas such a scenario can be avoided. Therefore BEC can be formed in a dilute and ultracold Bose gases. The gas is considered dilute if the characteristic length of the interaction l_{int} is much smaller than the average distance of the bosons, thus $l_{int}^3 n \ll 1$. In a dilute gas the bosons are weakly interacting through two-particle interactions. BEC can form in a dilute, non-ideal Bose gas, however the condensate fraction is smaller and the critical temperature is again altered [25], [26], [69], [15]. Experimentally, BEC has been realized first by different groups in ^{87}Rb ([1], [30], [19]), and in ^{23}Na ([16], [31]), in ^7Li ([10]).

3.1. Mean field approximation, the Gross-Pitaevskii equation

The static configuration of N interacting scalar bosons placed in the external potential V_{ext} in a second quantized formalism is characterized [15] by the Hamiltonian operator

$$\begin{aligned} \hat{H} = & \int d\mathbf{r}' \hat{\Psi}^+(\mathbf{r}') \left[-\frac{\hbar^2}{2m} \Delta' + V_{ext}(\mathbf{r}') \right] \hat{\Psi}(\mathbf{r}') \\ & + \frac{1}{2} \int d\mathbf{r}' d\mathbf{r}'' \hat{\Psi}^+(\mathbf{r}') \hat{\Psi}^+(\mathbf{r}'') V_{self}(\mathbf{r}' - \mathbf{r}'') \hat{\Psi}(\mathbf{r}') \hat{\Psi}(\mathbf{r}''). \end{aligned} \quad (10)$$

The operators (singled out by hats) are taken in the *Schrödinger picture*.¹ The boson field operators $\hat{\Psi}(\mathbf{r}')$ and $\hat{\Psi}^+(\mathbf{r}')$ annihilate and create a particle at the position \mathbf{r}' , while Δ' is the 3-dimensional Laplacian with respect to the coordinates \mathbf{r}' . The *repulsive*, two-body interatomic potential is

$$V_{self} = \lambda \delta(\mathbf{r} - \mathbf{r}') \quad (11)$$

with

$$\lambda = \frac{4\pi\hbar^2 a}{m} \quad (12)$$

¹The Hamiltonian operator coincides in the Schrödinger and Heisenberg pictures since it does not depend explicitly on time.

a self-coupling constant, given in terms of the scattering length a .

The field operator $\hat{\Psi}(\mathbf{r})$ is decomposed in terms of the single-particle annihilation operators \hat{a}_α as

$$\hat{\Psi}(\mathbf{r}) = \sum_{\alpha} \Psi_{\alpha}(\mathbf{r}) \hat{a}_{\alpha}, \quad (13)$$

where Ψ_{α} is the wave function of single-particle state $|\alpha\rangle$. The summation is taken over the single-particle state. The functions Ψ_{α} are orthonormal and form a complete set of single-particle wave functions, i.e.

$$\sum_{\alpha} \Psi_{\alpha}(\mathbf{r}) \Psi_{\alpha}^*(\mathbf{r}') = \delta(\mathbf{r} - \mathbf{r}'), \quad (14)$$

where a star denotes the complex conjugation. Denoting the particle numbers in some state (labeled α) by n_{α} , the bosonic annihilation \hat{a}_{α} and creation \hat{a}_{α}^+ operators act on the Fock space as

$$\hat{a}_{\alpha} |n_0, n_1, \dots, n_{\alpha}, \dots\rangle = \sqrt{n_{\alpha}} |n_0, n_1, \dots, n_{\alpha} - 1, \dots\rangle, \quad (15)$$

$$\hat{a}_{\alpha}^+ |n_0, n_1, \dots, n_{\alpha}, \dots\rangle = \sqrt{n_{\alpha} + 1} |n_0, n_1, \dots, n_{\alpha} + 1, \dots\rangle, \quad (16)$$

and satisfy the following commutation relations:

$$[\hat{a}_{\alpha}, \hat{a}_{\beta}^+] = \delta_{\alpha\beta}, \quad [\hat{a}_{\alpha}, \hat{a}_{\beta}] = 0, \quad [\hat{a}_{\alpha}^+, \hat{a}_{\beta}^+] = 0. \quad (17)$$

The numbers n_{α} are the eigenvalues of the operator $n_{\alpha} = \hat{a}_{\alpha}^+ \hat{a}_{\alpha}$. The commutation relations

$$[\hat{\Psi}(\mathbf{r}), \hat{\Psi}^+(\mathbf{r}')] = \delta(\mathbf{r} - \mathbf{r}'), \quad [\hat{\Psi}(\mathbf{r}), \hat{\Psi}(\mathbf{r}')] = 0, \quad [\hat{\Psi}^+(\mathbf{r}), \hat{\Psi}^+(\mathbf{r}')] = 0 \quad (18)$$

for the field operators follow from (17) and (14).

Since the Hamiltonian operator is time-independent, the boson field operator $\hat{\Psi}(\mathbf{r}, t)$ in the *Heisenberg picture* is

$$\begin{aligned} \hat{\Psi}(\mathbf{r}, t) &= e^{i\hat{H}t/\hbar} \hat{\Psi}(\mathbf{r}) e^{-i\hat{H}t/\hbar} = \sum_{\alpha} \Psi_{\alpha}(\mathbf{r}) e^{i\hat{H}t/\hbar} \hat{a}_{\alpha} e^{-i\hat{H}t/\hbar} \\ &= \sum_{\alpha} \Psi_{\alpha}(\mathbf{r}) \hat{a}_{\alpha}(t), \end{aligned} \quad (19)$$

with

$$\hat{a}_{\alpha}(t) = e^{i\hat{H}t/\hbar} \hat{a}_{\alpha} e^{-i\hat{H}t/\hbar}. \quad (20)$$

Similar equations are valid for the respective adjoint operators $\hat{\Psi}^+(\mathbf{r}, t)$, $\hat{a}_{\alpha}^+(t)$. The field operators obeys the Heisenberg equation, i.e.:

$$\begin{aligned} i\hbar \frac{\partial}{\partial t} \hat{\Psi}(\mathbf{r}, t) &= [\hat{\Psi}(\mathbf{r}, t), \hat{H}] \\ &= \left[-\frac{\hbar^2}{2m} \Delta + V_{ext}(\mathbf{r}) + \lambda \hat{\Psi}^+(\mathbf{r}, t) \hat{\Psi}(\mathbf{r}, t) \right] \hat{\Psi}(\mathbf{r}, t). \end{aligned} \quad (21)$$

Instead Eq. (21), it is effective computationally to use a *mean-field approximation*. The basic idea [9] is to separate the BEC contribution in the field operator as

$$\hat{\Psi}(\mathbf{r}, t) = \Psi_0(\mathbf{r}) \hat{a}_0(t) + \hat{\Psi}'(\mathbf{r}, t), \quad (22)$$

where the zero subscript denotes the ground-state and $\hat{\Psi}'(\mathbf{r}, t)$ carries the effects of the excited states. BEC occurs when the number of particles $n_0(t)$ in the condensate becomes very large, hence the states with $n_0(t)$ and $n_0(t) + 1$ correspond to the same configuration. In this case $\hat{a}_0(t) \approx \hat{a}_0^+(t) \approx \sqrt{n_0(t)}$ and the expectation value of the BEC contribution is

$$\psi(\mathbf{r}, t) = \sqrt{n_0(t)} \Psi_0(\mathbf{r}) , \quad (23)$$

the wave function of the condensate. By comparison the contribution from the non-condensed part is small, therefore $\hat{\Psi}'(\mathbf{r}, t)$ represents a perturbation with a negligible expectation value in the leading order approximation.

The probability density

$$\rho(\mathbf{r}, t) = |\psi(\mathbf{r}, t)|^2 , \quad (24)$$

by the choice $\int d\mathbf{r} |\Psi_0(\mathbf{r})|^2 = 1$ is normalized to

$$n_0(t) = \int d\mathbf{r} \rho(\mathbf{r}, t) , \quad (25)$$

such that $\rho(\mathbf{r}, t)$ also represents the number density of the condensate.

In the leading order approximation (neglecting the contribution of the excited states) Eq. (21) becomes

$$i\hbar \frac{\partial}{\partial t} \psi(\mathbf{r}, t) = \left[-\frac{\hbar^2}{2m} \Delta + V_{ext}(\mathbf{r}) + \lambda \rho(\mathbf{r}, t) \right] \psi(\mathbf{r}, t) , \quad (26)$$

known as the Gross-Pitaevskii equation [27], [28], [58] which describes the Bose-Einstein condensate in the mean-field approximation.

3.2. Madelung hydrodynamic equations

In order to find a solution of Eq. (26) it is worth to use the Madelung representation of complex wave-functions [43], [73]:

$$\psi(\mathbf{r}, t) = \sqrt{\rho(\mathbf{r}, t)} \exp \left[\frac{i}{\hbar} S(\mathbf{r}, t) \right] , \quad (27)$$

where the real-valued phase $S(\mathbf{r}, t)$ has the dimension of an action. The real part of Eq. (26) gives

$$\frac{\partial S}{\partial t} + \frac{1}{2m} (\nabla S)^2 + \lambda \rho + V_{ext} + V_Q = 0 , \quad (28)$$

corresponding to a generalized Hamilton-Jacobi equations with quantum correction potential

$$V_Q = -\frac{\hbar^2}{2m} \frac{\Delta \sqrt{\rho}}{\sqrt{\rho}} . \quad (29)$$

The imaginary part of (26) becomes a continuity equation

$$\frac{\partial \rho}{\partial t} + \nabla \cdot (\rho \mathbf{v}) = 0 , \quad (30)$$

while the gradient of (28) gives

$$m\rho \left[\frac{\partial \mathbf{v}}{\partial t} + (\mathbf{v} \cdot \nabla) \mathbf{v} \right] = -\nabla p - \rho \nabla V_{ext} - \rho \nabla V_Q . \quad (31)$$

Here we have introduced the notations

$$\mathbf{v} = \frac{\nabla S(\mathbf{r})}{m} , \quad (32)$$

and

$$p = \frac{\lambda}{2} \rho^2 . \quad (33)$$

The i th component of the last term of Eq. (31) can be rewritten as [2]

$$\rho \nabla_i V_Q = \sum_j \nabla_j \sigma_{ij}^Q , \quad (34)$$

where

$$\sigma_{ij}^Q = -\frac{\hbar^2}{4m} \rho \nabla_i \nabla_j \ln \rho . \quad (35)$$

Eqs. (30) and (31) correspond to the usual continuity and Euler equations of fluid mechanics, with \mathbf{v} the classical velocity field, p the pressure and σ_{ij}^Q representing a quantum correction to the stress tensor. Eqs. (30) and (31) are the Madelung hydrodynamic equations.

3.3. Self-gravitating, spherically symmetric BEC distribution in the Thomas-Fermi approximation

A stationary state ψ is

$$\psi(\mathbf{r}, t) = \sqrt{\rho(\mathbf{r})} \exp \left(\frac{i\mu}{\hbar} t \right) , \quad (36)$$

with $\mu = \text{const}$. Then the continuity equation is automatically satisfied while Eq. (28) leads to

$$V_{ext} + V_Q + \lambda \rho = \mu . \quad (37)$$

The quantum correction potential V_Q has significant contribution only close to the bound [75], therefore it can be neglected as compared to the self-interaction term $\lambda \rho$. This *Thomas-Fermi approximation* becomes increasingly accurate with an increasing number of particles [42].

If $V_{ext}(\mathbf{r})/m$ is the Newtonian gravitational potential created by the condensate, it satisfies the Poisson equation:

$$\Delta \frac{V_{ext}}{m} = 4\pi G \rho_{BEC} , \quad (38)$$

where $\rho_{BEC} = m\rho$ is the mass density of the BEC and G is the gravitational constant.

The Laplacian of Eq. (37) and Eq. (38) give

$$\Delta \rho_{BEC} + \frac{4\pi G m^2}{\lambda} \rho_{BEC} = 0 . \quad (39)$$

For a spherical symmetric distribution this simplifies to

$$\frac{d^2 (r \rho_{BEC})}{dr^2} + \frac{4\pi G m^2}{\lambda} (r \rho_{BEC}) = 0, \quad (40)$$

with the solution [75], [6]:

$$\rho_{BEC}(r) = \rho_{BEC}^{(c)} \frac{\sin kr}{kr}, \quad (41)$$

where

$$k = \sqrt{\frac{Gm^3}{\hbar^2 a}} \quad (42)$$

and $\rho_{BEC}^{(c)} \equiv \rho_{BEC}(0)$ is a central density, determined from the normalization condition (21) as

$$\rho_{BEC}^{(c)} = \frac{n_0 m k^3}{4\pi^2}. \quad (43)$$

The exists of a central finite density is exactly the required feature which represents an advantage over cuspy dark matter profiles derived from N-body simulation.

At the end of this subsection we comment on the validity of the Thomas-Fermi approximation. The quantum correction potential (29), rewritten in spherical coordinates and inserted into Eq. (37) generates constant and ρ_{BEC}^{-2} terms, while the contribution of the self-interaction term is proportional to ρ_{BEC} . Close to the boundary R_{BEC} therefore the Thomas-Fermi approximation fails. Multiplying Eq. (37) by $(\rho_{BEC}/\rho_{BEC}^{(c)})^2$, with ρ_{BEC} given by Eq. (41), and integrating on the range $r \in [0, R_{BEC}]$ gives the global weight of these terms as \hbar^2/km for the V_Q term and $\hbar^2 a n_0$ for the self-interaction term, respectively. Therefore the Thomas-Fermi approximation holds valid for $n_0 \gg 1/ka$, a condition also obtained by a different method in Ref. [75].

3.4. BEC dark matter halo

In the following, we investigate the possibility that dark matter halos are Bose-Einstein condensates [72].

The size of the BEC galactic dark matter halo is defined by $\rho(R_{BEC}) = 0$, giving $k = \pi/R_{BEC}$, i.e.

$$R_{BEC} = \pi \sqrt{\frac{\hbar^2 a}{Gm^3}}. \quad (44)$$

The mass profile of the BEC halo is then given by

$$\begin{aligned} m_{BEC}(r) &= 4\pi \int_0^r \rho_{BEC}(r) r^2 dr \\ &= \frac{4\pi \rho_{BEC}^{(c)}}{k^2} r \left(\frac{\sin kr}{kr} - \cos kr \right). \end{aligned} \quad (45)$$

The contribution of the BEC halo to the velocity profile of the particles moving on circular orbit under Newtonian gravitational force is

$$v^2(r) = \frac{4\pi G \rho_{BEC}^{(c)}}{k^2} \left(\frac{\sin kr}{kr} - \cos kr \right). \quad (46)$$

This has to be added to the respective baryonic contribution.

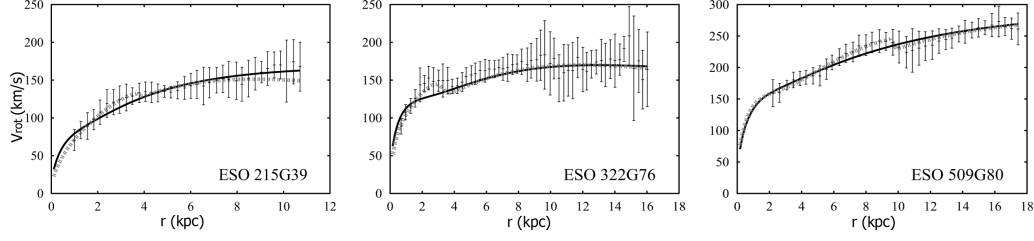


Figure 1. Best fit curves for the HSB galaxy sample. The dashed lines hold in the baryonic matter + BEC model, while the solid lines in the baryonic matter + NFW model. In the second and third example the curves run very close to each other.

4. CONFRONTING THE BEC MODEL WITH ROTATION CURVE DATA

In order to test the validity of the BEC dark matter model, we confront the rotation curve data of a sample of 3 High Surface Brightness (HSB) galaxies, 3 Low Surface Brightness (LSB) galaxies and 3 dwarf galaxies, with both the NFW dark matter and the BEC density profiles.

The commonly used NFW model is based on the numerical simulations of dark-matter halos in the Λ CDM framework [52]. The mass density profile is given by

$$\rho_{NFW}(r) = \frac{\rho_s}{(r/r_s)(1 + r/r_s)^2}, \quad (47)$$

where there are two fit parameters ρ_s and r_s .

The mass within a sphere with radius $r = yr_s$ is then given by

$$M(r) = 4\pi\rho_sr_s^3 \left[\ln(1 + y) - \frac{y}{1 + y} \right], \quad (48)$$

where y is a dimensionless radial coordinate.

4.1. HIGH SURFACE BRIGHTNESS GALAXIES

We follow the method described in Ref. [24]. In a High Surface Brightness galaxy we decompose the baryonic component into a thin stellar disk and a spherically symmetric bulge. We assume that the mass distribution of the bulge component follows the deprojected luminosity distribution, the proportionality factor being the mass-to-light ratio. We estimate the bulge parameters from a Sérsic $r^{1/n}$ bulge model, fitted to the optical I-band galaxy light profiles.

Galaxy	D	$I_{0,b}$	n	r_0	r_b	$I_{0,d}^{HSB}$	h^{HSB}
	Mpc	mJy/arcsec ²		kpc	kpc	mJy/arcsec ²	kpc
ESO215G39	61.29	0.1171	0.6609	0.78	2.58	0.0339	4.11
ESO322G76	64.28	0.2383	0.8344	0.91	4.50	0.0251	5.28
ESO509G80	92.86	0.2090	0.7621	1.10	4.69	0.0176	11.03

Table 1. The distances (D) and the photometric parameters of the 3 HSB galaxy sample. Bulge parameters: the central surface brightness ($I_{0,b}$), the shape parameter (n), the characteristic radius (r_0) and radius of the bulge (r_b). Disk parameters: central surface brightness ($I_{0,d}^{HSB}$) and length scale (h^{HSB}) of the disk.

4.1.1. Bulge contribution

The surface brightness profile of the spheroidal bulge component of each galaxy is described by a generalized Sérsic function [71]

$$I_b(r) = I_{0,b} \exp \left[- \left(\frac{r}{r_0} \right)^{1/n} \right], \quad (49)$$

where $I_{0,b}$ is the central surface brightness of the bulge, r_0 is its characteristic radius and n is the shape parameter of the magnitude-radius curve.

The respective mass over luminosity is the mass-to-light ratio, for the Sun being $\gamma_\odot = 5133 \text{ kg W}^{-1}$. In what follows, the mass-to-light ratio of the bulge σ will be given in units of γ_\odot (solar units), while the masses in units of the solar mass $M_\odot = 1.98892 \times 10^{30} \text{ kg}$. The radial distribution of visible mass is given by the radial distribution of light obtained from the bulge-disk decomposition. Thus the mass of the bulge within the projected radius r is proportional to the surface brightness encompassed by this radius:

$$M_b(r) = \sigma \frac{\mathcal{N}(D)}{F_\odot} 2\pi \int_0^r I_b(r) r dr,$$

where $F_\odot(D)$ is the apparent flux density of the Sun at a distance D Mpc, $F_\odot(D) = 2.635 \times 10^{6-0.4f_\odot} \text{ mJy}$, with $f_\odot = 4.08 + 5 \lg(D/1 \text{ Mpc}) + 25 \text{ mag}$, and

$$\mathcal{N}(D) = 4.4684 \times 10^{-35} D^{-2} \text{ m}^{-2} \text{ arcsec}^2. \quad (50)$$

Therefore the contribution of the bulge to the rotational velocity is

$$v_b^2(r) = \frac{GM_b(r)}{r}. \quad (51)$$

4.1.2. Disk contribution

In a spiral galaxy, the radial surface brightness profile of the disk exponentially decreases with the radius [22]

$$I_d(r) = I_{0,d}^{HSB} \exp\left(-\frac{r}{h^{HSB}}\right), \quad (52)$$

where $I_{0,d}^{HSB}$ is the disk central surface brightness and h^{HSB} is a characteristic disk length scale. The contribution of the disk to the circular velocity is [22]

$$v_d^2(x) = \frac{GM_D^{HSB}}{2h^{HSB}} x^2 (I_0 K_0 - I_1 K_1), \quad (53)$$

where I_n and K_n are the modified Bessel functions calculated at $x/2 = r/2h^{HSB}$ and M_D^{HSB} is the total mass of the disk.

4.1.3. Confrontation with rotation curve data

Therefore the rotational velocity in a HSB galaxy receives the following contributions

$$v_{tg}^2(x) = v_b^2(x) + v_d^2(x) + v_{DM}^2(x).$$

We confront the BEC+baryonic model with (HI and H_α) rotation curve data of 3 galaxies already employed in Ref. [24], which were extracted from a larger sample given in Ref. [54] by requiring i) sufficient and accurate data for each galaxy and ii) manifest spherical structure of the bulge (no visible rings and bars). For comparison, the NFW+baryonic model is also tested on the same sample, by plotting the respective rotation curves in both models. The results are represented on Fig. 1.

For the HSB galaxy sample we have derived the best fitting values of the baryonic model parameters $I_{0,b}$, n , r_0 , r_b , $I_{0,d}^{HSB}$ and h^{HSB} from the available photometric data. The BEC and NFW parameters were calculated (together with the corresponding baryonic parameters) by fitting these models to the rotation curve data. These are collected in the tables 1 and 2.

4.2. LOW SURFACE BRIGHTNESS GALAXIES

Low Surface Brightness (LSB) galaxies are characterized by a central surface brightness at least one magnitude fainter than the night sky. These galaxies form the most unevolved class of galaxies [36] and have low star formation rates as compared to their HSB counterparts [49]. LSB galaxies show a wide spread of colours ranging from red to blue [53] and represent a large variety of properties and morphologies. Although the most commonly observed LSB galaxies are dwarfs, a significant fraction of LSB galaxies are large spirals [4].

Our model LSB galaxy consists of a thin stellar+gas disk and a cold dark matter component in a form of BEC. The disk component is the same as at the HSB galaxies, the surface brightness profile is [22]

$$I_d(r) = I_{0,d}^{LSB} \exp\left(-\frac{r}{h^{LSB}}\right),$$

Galaxy	$\sigma(\text{BEC})$	$M_D^{\text{HSB}}(\text{BEC})$	R_{BEC}	$\rho_{\text{BEC}}^{(c)}$	$\chi_{\min}^2(\text{BEC})$	$\sigma(\text{NFW})$	$M_D^{\text{HSB}}(\text{NFW})$	r_s	ρ_s	$\chi_{\min}^2(\text{NFW})$	1σ
	\odot	$10^{10} M_\odot$	kpc	10^{-21}kg/m^3		\odot	$10^{10} M_\odot$	kpc	10^{-24}kg/m^3		
ESO215G39	0.7	4.96	50	0.2	22.9	0.6	3.84	187	14.7	22.22	34.18
ESO322G76	0.8	9.08	5	0.5	48.31	0.9	8.29	920	0.7	49.02	53.15
ESO509G80	1.3	52.02	7	1.6	19.77	0.9	11	22	800	33.48	36.3

Table 2. The best fit parameters and the minimum values (χ_{\min}^2) of the χ^2 statistics for the 3 HSB galaxies. Columns 2-5 give the BEC model parameters (radius R_{BEC} and central density $\rho_{\text{BEC}}^{(c)}$ of the BEC halo) and the corresponding baryonic parameters (mass-to-light ratio $\sigma(\text{BEC})$ of the bulge and total mass of the disk $M_D^{\text{HSB}}(\text{BEC})$). Columns 7-10 give the NFW model parameters (scale radius r_s and characteristic density ρ_s of the halo) and the corresponding baryonic parameters (mass-to-light ratio $\sigma(\text{NFW})$ of the bulge and total mass of the disk $M_D^{\text{HSB}}(\text{NFW})$). The 1σ confidence levels are shown in the last column (these are the same for both models). For all galaxies χ_{\min}^2 are within the 1σ confidence level. Both model fittings give similar χ_{\min}^2 values.

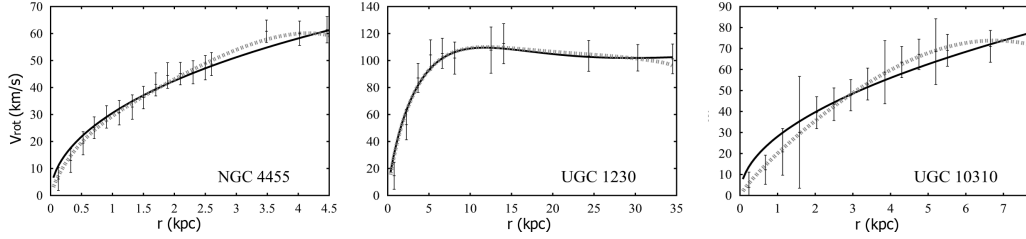


Figure 2. Best fit curves for the 3 LSB galaxies (the dashed lines show the combined BEC+baryonic model, the solid lines show the combined NFW+baryonic profiles).

where $I_{0,d}^{\text{LSB}}$ is the central surface brightness and h^{LSB} is the disk length scale. We can calculate the disk contribution to the circular velocity as

$$v_d^2(r) = \frac{GM_D^{\text{LSB}}}{2h^{\text{LSB}}} x^2 (I_0 K_0 - I_1 K_1), \quad (54)$$

similarly to the case of HSB galaxies.

Therefore for a generic projected radius r , the rotational velocity in this combined model can be written as

$$v_{tg}^2(r) = v_d^2(r) + v_{DM}^2.$$

We follow the analysis of the BEC model with the rotation curves of 3 LSB galaxies taken from a larger sample [17]. These high quality rotation curve data are based on both HI and $\text{H}\alpha$ measurements. From a χ^2 -test we have determined the model parameters in both the BEC+baryonic and NFW+baryonic models, these are shown in Table 3. The fitted curves are represented on Fig. 2.

4.3. DWARF GALAXIES

Dwarf galaxies are the most common galaxies in the observable Universe. About 85% of the known galaxies in the Local Volume are dwarfs [38]. Dwarf galaxies are defined as

Galaxy	D	h^{LSB}	$M_D^{LSB}(BEC)$	$\rho_{BEC}^{(c)}$	R_{BEC}	$\chi^2_{min}(BEC)$	$M_D^{LSB}(NFW)$	ρ_s	r_s	$\chi^2_{min}(NFW)$	1σ
	Mpc	kpc	$10^9 M_\odot$	$10^{-21} kg/m^3$	kpc		$10^9 M_\odot$	$10^{-24} kg/m^3$	kpc		
NGC 4455	6.8	0.7	0.236	1.4	5.6	9.4	0	62	39	30.37	18.11
UGC 1230	51	4.5	27	0.1	27.7	19.86	26.2	2	291	19.84	8.17
UGC 10310	15.6	1.9	0.412	1	7.7	2.68	0	3	660	28.78	13.74

Table 3. The best fit BEC and NFW parameters of the 3 LSB galaxies.

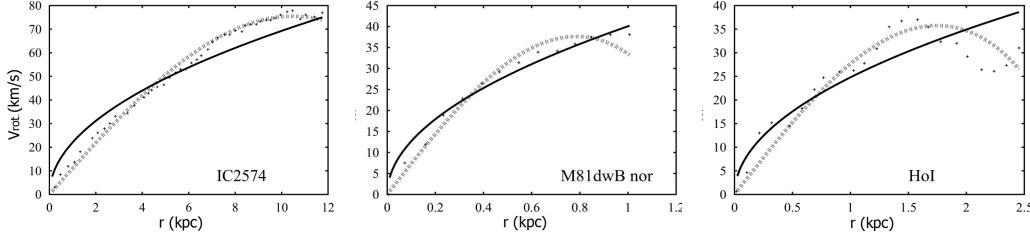


Figure 3. The best fit curves for the dwarf galaxy sample. The BEC+baryonic model (dashed curves) gives a better fit in all cases than the NFW+baryonic model (solid lines). In both cases the fit was performed with the same baryonic model.

galaxies having an absolute magnitude fainter than $M_B \sim -16$ mag, and more extended than globular clusters [74].

The formation history of dwarf galaxies is not well-understood. According to [76], dwarf galaxies formed at the centers of subhalos orbiting within the halos of giant galaxies. Five main classes of dwarf galaxies are distinguished based on their optical appearance: dwarf ellipticals, dwarf irregulars, dwarf spheroidals, blue compact dwarfs, and dwarf spirals. The last one type can be regarded as the very small end of spirals [48].

All dwarf galaxies have central velocity dispersions $\sim 6 \div 25$ km/s [47]. If the systems are in dynamic equilibrium, the mass derived from these velocity dispersions is much larger than the derived stellar mass. Therefore the dwarf galaxies are among the darkest objects ever observed in the Universe, hence they play an important role in the study of dark matter distribution on small scales. As dwarf galaxies are supposed to be dark matter dominated at all radii, they are ideal objects to prove or falsify various alternative gravity theories [12].

To test the BEC model, we have selected a sample of 3 dwarf galaxies for which high resolution rotation curves are available. We performed the rotation curve fitting with the BEC+baryonic and the NFW+baryonic models, respectively. The baryonic components were the same as in the case of LSB galaxies. However, the length scales of the stellar disks are not available for this sample, therefore they are calculated from χ^2 minimization, too. This comparison allows us to test the viability of our model.

For the investigated dwarf galaxies the best fit BEC and NFW parameters are shown in Table 4 and the fitted rotation curves are represented in Fig. 3.

Galaxy	$h^{dwarf}(BEC)$ kpc	$M_D^{dwarf}(BEC)$ $10^9 M_\odot$	$\rho_{BEC}^{(c)}$ 10^{-24} kg/m^3	R_{BEC} kpc	$\chi_{\min}^2(BEC)$	$h^{dwarf}(NFW)$ kpc	$M_D^{dwarf}(NFW)$ $10^9 M_\odot$	ρ_s 10^{-24} kg/m^3	r_s kpc	$\chi_{\min}^2(NFW)$	1σ
IC 2574	1.2	0.1122	0.4	13	68.47	7.9	28.44	0	0	714.73	44.74
Hol	0.2	0.0107	3.6	1.9	95.26	0.9	0.533	0	0	241.30	20.27
M81dwB nor	0.9	1.023	3.7	0.7	6.19	0.7	0.705	0	0	8.4	10.42

Table 4. The best fit BEC+baryonic and NFW+baryonic parameters for the dwarf galaxy sample.

5. CONCLUSION

We presented here a comprehensive introduction into the theory of Bose-Einstein condensates (BEC), with emphasis on a spherically symmetric self-gravitating BEC in the Thomas-Fermi approximation.

In the BEC model, large-scale structures like clusters or superclusters of galaxies form similarly as in the Cold Dark Matter model with cosmological constant, thus all predictions of the standard model at large scales are well reproduced [44]. Moreover the BEC model can explain the collisions of galaxy clusters [41] and the acoustic peaks of the cosmic microwave background [66].

Such a BEC has been proposed recently as a galactic dark matter model and has been partially tested by confronting with rotation curve data in Refs. [18, 33, 65].

Here we have performed a much thorough test of this BEC dark matter model by confronting with a sample of 3 HSB, 3 LSB and 3 dwarf galaxies and also comparing the model predictions with those of the widely accepted NFW dark matter model. We incorporated in all cases realistic baryonic models, taking into account the particularities of the respective galaxy types. Beside the rotation curve data for the HSB galaxies, the surface photometry data was also available. The galaxies have different luminosities, disk length-scales and surface brightnesses. Most of the rotation curve data were densely distributed and uniform in quality.

We have also fitted the rotation curves of a sample of 3 *dwarf galaxies* with both the BEC+baryonic and NFW+baryonic dark matter models. Since dwarf galaxies are supposed to be dark matter dominated, they provide the strongest test of the compared models. The results are shown in Fig. 3. In all cases, the BEC dark matter model gave better results than the NFW dark matter model.

For all galaxy types we have determined the BEC parameters ρ_{BEC} , R_{BEC} , given in Tables 2, 3, and 4.

For the investigated galaxies, we decomposed the circular velocity into its baryonic and dark matter contributions: $v_{\text{model}}^2(r) = v_{\text{baryonic}}^2 + v_{DM}^2$. The dark matter contribution to the velocity is given by Eq. (46). Then the rotation curves are χ^2 best-fitted with the baryonic parameters and the parameters of the two dark matter halo models (BEC and NFW).

For the sample of *HSB galaxies* we found a remarkably good agreement of both dark matter models with the observations. The quality of the fits of the BEC and NFW models with the rotation curve data was comparable.

For the sample of *LSB galaxies*, the BEC model gave a slightly better fit than the NFW model. We additionally found that adding the baryonic component results in a better fit than the one presented in [65] for the pure BEC model.

We note that due to the sharp cut-off of the BEC halos the very distant behaviour of the universal rotation curves (URCs) [57] is not expected to be reproduced, hence a modification of the BEC model on large distances would be desirable.

One suggestion takes into account the effects of the finite dark matter temperature on the properties of the dark matter halos. However it turned out, that these effects do not play a significant role in the description of the dark matter halo density profiles [35]. A possible solution is including vortex lattices in the halo [59, 78]. When a BEC is rotated at a rate exceeding some critical frequency, quantized vortices can be formed. This vortex lattice can influence the galactic rotation curve and provide a flat velocity profile with oscillatory structure [65, 77].

We conclude that the BEC dark matter model is well supported by rotation curve data and it certainly deserves further attention.

PACS 05.45-a, 52.35.Mw, 96.50.Fm. **Keywords:** Dark matter halos.

References

- [1] Anderson, M.H., Ensher, J.R., Matthews, M.R., Wieman, C.E., Cornell, E.A., 1995, *Science* **269**, 198
- [2] Barcelo, C., Liberati, S., Visser, M., 2011, *Class. Quant. Grav.* **18**, 1137
- [3] Battaner, E., Garrido, J.L., Membrado, M., Florido, E., 1992 *Nature*, **360**, 6405, p. 652
- [4] Beijersbergen, M., de Blok, W.J.G., van der Hulst, J.M., 1999, *A&A* **351**, 903
- [5] Bertolami, O., Boehmer C.G., Harko, T., Lobo, F.S.N., 2007, *Phys. Rev. D* **75**, 104016
- [6] Boehmer, C.G., Harko, T., 2007b, *JCAP* **06**, 025
- [7] Boehmer, C.G., Harko, T., Lobo, F.S.N., 2008, *Astropart. Phys.*, **29**, 386
- [8] Boehmer, C.G., Harko, T., 2007a, *MNRAS* **379**, 2007
- [9] Bogoliubov, N., 1947, *J. Phys. USSR* **11**, 23
- [10] Bradley, C.C., Sackett, C.A., Tollett, J.J., Hulet, R.G., 1995, *Phys. Rev. Lett.* **75**, 1687

- [11] Burkert, A., 1997, "Aspects of Dark Matter in Astro-and Particle Physics"
- [12] Capozziello, S., Cardone, V.F., Troisi, A., 2007, MNRAS **375**, 1423
- [13] Chavanis, P.-H., 2011, Phys. Rev. D **84**, 043531
- [14] Chavanis, P.-H., Delphini, L., 2011, Phys. Rev. D **84**, 043532
- [15] Dalfovo, F., Giorgini, S., Pitaevskii, L.P., Stringari, S., 1999, Rev. Mod. Phys. **71**, 463
- [16] Davis, K.B., Mewes, M.-O., Andrews, M.R., van Druten, N.J., Durfee, D.S., Kurn, D.M., Ketterle, W., 1995, Phys. Rev. Lett. **75**, 3969
- [17] de Blok W.J.G., Bosma A., 2002, A&A **385**, 816
- [18] Dwornik, M., Keresztes, Z., Gergely, L.Á., 2013, [arXiv:1301.6614]
- [19] Ernst, U., Marte, A., Schreck, F., Schuster, J., Rempe, G., 1998, Europhys. Lett. **41**, 1
- [20] Evans, N.W., 2001, Proc. 3rd International Workshop on the Identification of Dark-Matter. World Sci., Singapore, p. 85
- [21] Fukuyama, T., Morikawa, M., 2006, Progress of Theoretical Physics **115**, 1047
- [22] Freeman, K.C., 1970, ApJ **160**, 811
- [23] Gentile, G., Famaey, B., Zhao, H., Salucci, P., 2009, Nature **461**, 627
- [24] Gergely, L.Á., Harko, T., Dwornik, M., Kupi, G., Keresztes, Z., 2011, MNRAS **415**, 3275
- [25] Giorgini, S., Pitaevskii, L., Stringari, S., 1996, Phys. Rev. A **54**, R4633
- [26] Glaum, K., Pelster, A., Kleinert, H., Pfau, T., 2007, Phys. Rev. Lett. **98**, 080407
- [27] Gross, E.P., 1961, Nuovo Cimento **20**, 454
- [28] Gross, E.P., 1963, J. Math. Phys. **4**, 195
- [29] Grossmann, S., Holthaus, M., 1995, Zeit. f. Naturforsch. **50a**, 921; Phys. Lett. A **208**, 188
- [30] Han, D.-J., Wynar, R.H., Courteille Ph., Heinzen D.J., 1998, Phys. Rev. A **57**, R4114
- [31] Hau, L.V., Busch, B.D., Liu, C. Z. Dutton, Burns, M.M., Golovchenko, J.A., 1998, Phys. Rev. A **58**, R54
- [32] Haugerud, H., Haugset, T., Ravndal, F., 1997, Phys. Lett. A **225**, 18
- [33] Harko, T., 2011a, JCAP **05**, 022
- [34] Harko, T., 2011b, MNRAS **413**, 3095
- [35] Harko, T., Madarassy, E. J. M., 2011 [arXiv:1110.2829v1]

- [36] Impey, C., Bothun, G., 1997, ARA&A. **35**, 267
- [37] Jalocha, J., Bratek, L., Kutschera, M., Skindzier, P., 2010, MNRAS **406**, 2805-2816
- [38] Karachentsev, I. D., Karachentseva, V. E., Huchtmeier, W. K., Makarov, D. I., 2004, AJ **127**, 2031
- [39] Ketterle, W., van Druten N.J., 1996, Phys. Rev. A **54**, 656
- [40] Kristen, K., Toms, D.J., 1996, Phys. Rev A **54**, 4188
- [41] Lee, J.W., Lim, S., Choi, D., 2008, [arXiv:0805.3827v1]
- [42] Lieb, E.H., Seiringer, R., Yngvason, Y., 2000, Phys. Rev. A **61**, 043602
- [43] Madelung, E., 1926, Zeitschrift für Physik **38**, 322
- [44] Magana, J., Matos, T., Robles, V. H., Suarez, A., 2012, Proceedings of the XIII Mexican Workshop on Particles and Fields [arXiv:1201.6107v1]
- [45] Mak, M. K., Harko, T., 2004, Phys. Rev. D **70** , 024010
- [46] Mannheim P. D., 1997, AJ **479**, 659
- [47] Mateo, M., 1998, ARA&A **36**, 435
- [48] Matthews, L. D. and Gallagher, J. S., 1997, AJ **114**, 5
- [49] McGaugh, S.S., 1994, ApJ **426**, 135
- [50] Milgrom, M., 1983, APJ **270**, 365
- [51] Moffat, J.W., Sokolov, I.Y., 1996, Phys. Lett. B **378**, 59
- [52] Navarro, J.F., Frenk, C.S., White, S.D.M., 1996, ApJ **462**, 563
- [53] O’Neil, K., Bothun, G.D., Schombert, J., Cornell, M.E., Impey, C.D., 1997, AJ **144**, 244
- [54] Palunas, P., Williams, T.B., 2000, AJ **120**, 2884
- [55] Padmanabhan, T., 2003, Phys. Repts. **380**, 235
- [56] Peebles, P. J. E., Ratra, B., 2003, Rev. Mod. Phys. **75**, 559
- [57] Persic, M., Salucci, P., Stel, F., 1996, MNRAS **281**, 27
- [58] Pitaevskii, L.P., 1961, Zh. Eksp. Teor. Fiz. **40**, 646 [Sov. Phys. JETP **13**, 451 (1961)]
- [59] Pitaevskii, L. P., Stringari S., 2003, Bose-Einstein Condensation, Oxford University Press Inc., New York.
- [60] Planck collaboration, 2013, [arXiv:1303.5076]

-
- [61] Planck collaboration, 2013, [arXiv:1303.5075]
- [62] Rahaman, F., Kalam, M., DeBenedictis, A., Usmani, A.A., Saibal, R., 2008, MNRAS **389**, 27
- [63] Rindler-Daller, T., Shapiro, P., 2011, [arXiv:1106.1256]
- [64] Roberts, M.D., 2004, Gen. Rel. Grav. **36**, 2423
- [65] Robles, V. H., Matos T., 2012, MNRAS **422**, 282-289
- [66] Rodriguez-Montoya, I., Magana, J., Matos, T., Perez-Lorezana, A., 2010, ApJ **721**, 1509
- [67] Sanders, R.H., 1984, A&A **136**, L21
- [68] Salucci, P., Persic, M., 1999, MNRAS **309**, 923
- [69] Schütte, M., Pelster, A., 2008, *Critical Temperature of a Bose-Einstein Condensate with $1/r$ Interactions*, Proceedings of the 9th International Conference, 23-28, September, 2007, Dresden, Germany, Eds. Janke W. and Pelster A., World Scientific Publishing Co. Pte. Ltd., 2008. ISBN #9789812837271, pp. 417-420
- [70] Sellwood, J.A., Kosowsky, A., 2000, ASP Conf. Ser. Vol. 240, Gas and Galaxy Evolution. Astron. Soc. Pac., San Francisco, p. 311
- [71] Sérsic, J.L., 1968, Atlas de Galaxias Australes, Cordoba, Argentina, Observatorio Astronomico
- [72] Sin, S.J., 1994, Phys. Rev. D **50**, 3650
- [73] Sonogo, S., 1991, Found. Phys. **21**, 1135
- [74] Tammann, G. A., 1994, Dwarf Galaxies in the Past, in Dwarf Galaxies, ESO Conference and Workshop Proc No. 49, Eds. G. Meylan and P. Prugniel, Paris, p. 3
- [75] Wang, X.Z., 2001, Phys. Rev D **64**, 124009
- [76] Wu, X., 2007, submitted to ApJ
- [77] Yu, R. P., Morgan M. J., 2002, Class. Quantum Grav. **19** L157
- [78] Zinner, N. T., 2011, [arXiv:1108.4290v1]